Three-Dimensional Composite Velocity Solutions for Subsonic/Transonic Flow

Raymond E. Gordnier*
Wright Laboratory, Wright-Patterson Air Force Base, Ohio 45433
and
Stanley G. Rubin†
University of Cincinnati, Cincinnati, Ohio 45221

A composite velocity procedure for the three-dimensional reduced Navier-Stokes equations is developed. In the spirit of matched asymptotic expansions, the velocity components are written as a combined multiplicative and additive composite of viscous like velocities (U, W) and pseudopotential or inviscid velocities (Φ_x, Φ_y, Φ_z). The solution procedure is then consistent with both asymptotic inviscid flow and boundary-layer theory. For transonic flow cases, the Enquist-Osher flux-biasing scheme developed for the full potential equation is used. A quasiconservation form of the governing equations is used in the shock region to capture the correct rotational behavior. This is combined with the standard nonconservation, non-entropy-generating form used in nonshock regions. The consistent strongly implicit procedure is coupled with plane relaxation to solve the discretized equations. The composite velocity procedure is applied to the solution of three-dimensional afterbody problems.

Introduction

As the field of computational fluid dynamics has matured, the need for solution procedures that can efficiently solve three-dimensional flows with complex viscous/inviscid interactions has become apparent. One technique for solving these problems is to obtain solutions to the time-dependent Navier-Stokes equations using the time asymptotic limit for the steady-state solution. While the rapid advances in computer technology have made this type of solution procedure possible, they are still costly in both computer time and resources.

The reduced Navier-Stokes (RNS) equations provide an attractive alternative to the full time-dependent Navier-Stokes equations for viscous/inviscid interacting flows. This set of equations has been developed to simulate large Reynolds number (Re) asymptotic behavior while retaining a single composite set of equations. The RNS equations are a composite of the full Euler and second-order boundary-layer systems. The terms neglected in the Navier-Stokes equations are higher order in Re in an appropriate "streamline" coordinate system.

The asymptotic nature of the RNS equations may be further exploited by the use of a composite representation for the flow velocities. In the composite velocity formulation, a combination of a multiplicative and additive composite is defined in the spirit of matched asymptotic expansions. Viscous or rotational velocities U and W and a pseudopotential or inviscid velocity (Φ_x, Φ_y, Φ_z) are specified. The composite velocity formulation is thus consistent with both asymptotic inviscid flow and boundary-layer theory. For inviscid flows, the continuity equation reduces to the full potential equation, and the momentum equations are identically satisfied. In viscous flow regions, the velocities are determined from the continuity equation and the axial and crossflow momentum equations. The normal momentum equation provides a viscous total pressure correction.

The splitting of the velocities into a composite of viscous and inviscid velocities provides several advantages over primitive variable formulations. Since the full potential equation is the basic equation for the inviscid flow in the composite procedure, the extensive knowledge base for solving this equation for transonic flows may be exploited when developing the solution procedure for the composite velocity system. In particular, techniques for transonic flow developed for the full potential equation may be applied to the composite velocity form of the RNS equations. The ability to identify viscous and inviscid velocities allows these terms to be treated numerically appropriate to the asymptotic character of the terms, i. e., marching of the viscous velocities representing the parabolic character of the boundary layer equations and central differencing for the inviscid velocities representing the elliptic nature of inviscid subsonic flow. For separated flows, the two-dimensional composite velocity formulation does not require upwinding in the separated region, and the three-dimensional formulation requires upwinding for only the azimuthal W_ξ convective derivative.

The composite velocity formulation has been applied previously for the two-dimensional Navier-Stokes equations for both incompressible[1] and compressible flows.[2-4] In previous work by the present authors, the composite velocity formulation was applied to the two-dimensional Euler and RNS equations.[5,6] These works have shown the ability of the composite velocity scheme to calculate laminar and turbulent flows accurately both with and without separation. Comparisons of the computed results have been made with both experimental and other numerical results. The purpose of the present work is to extend the composite velocity scheme to the solution of three-dimensional flows.

The composite velocity procedure is applied to the solution of nonaxisymmetric afterbody flows. Solutions to these types of problems can be very important in aft-fuselage-engine integration for fighter aircraft design. The complex viscous/inviscid interactions in these flows provide a computational challenge to any flow solver. The composite velocity procedure provides an efficient alternative to some of the Navier-Stokes procedures currently being used to solve these problems.[7,8]

Governing Equations

The governing equations to be solved are given by the three-dimensional, steady, compressible, RNS approximation.

Received July 12, 1989; revision received April 2, 1990.

*Visiting Scientist, MicroCraft, Inc. Member AIAA.
†Professor, Department of Aerospace Engineering and Engineering Mechanics. Associate Fellow AIAA.

These equations have been formulated for a general, nonorthogonal, curvilinear system of coordinates. This allows the use of appropriate streamline coordinate systems.

The governing equations are now given in their composite velocity formulation. In the spirit of matched asymptotic expansions, the flow velocities are written as

$$u = (U+1)(g^{11}\Phi_\xi + g^{12}\Phi_\eta + g^{13}\Phi_\zeta) = (U+1)u_e \tag{1a}$$

$$v = (g^{21}\Phi_\xi + g^{22}\Phi_\eta + g^{23}\Phi_\zeta) \tag{1b}$$

$$w = (U+1)(g^{31}\Phi_\xi + g^{32}\Phi_\eta + g^{33}\Phi_\zeta) + W = (U+1)w_e + W \tag{1c}$$

The composite representations of u and w, the axial and crossflow velocity components, contain two types of terms, irrotational pseudo potential velocities, e. g., Φ_ξ, Φ_η, and Φ_ζ and viscous velocities U and W. Since the change in v across the boundary layer is of the order of the boundary-layer thickness, the normal velocity is determined solely by the pseudo potential. While this composite form is motivated by boundary-layer theory, no additional restrictions result as all the terms of the RNS equations are still retained. This particular composite form also has the advantage that no additional unknowns are introduced, and the boundary conditions remain easy to implement.

By substituting Eqs. (1a–1c) into the RNS equations, the following system is obtained:

Continuity:

$$\frac{\partial}{\partial\xi}[\rho\sqrt{g}(U+1)u_e] + \frac{\partial}{\partial\eta}(\rho\sqrt{g}v) + \frac{\partial}{\partial\zeta}[\rho\sqrt{g}(U+1)w_e] + \frac{\partial}{\partial\zeta}(\rho\sqrt{g}W) = 0 \tag{2}$$

ξ-momentum equation:

$$\frac{1}{\rho\sqrt{g}}\left\{\frac{\partial}{\partial\xi}[\rho\sqrt{g}(U^2+U)u_e^2] + \frac{\partial}{\partial\eta}(\rho\sqrt{g}Uvu_e) + \frac{\partial}{\partial\zeta}[\rho\sqrt{g}(U^2+U)u_ew_e] + \frac{\partial}{\partial\zeta}(\rho\sqrt{g}UWu_e)\right\} + Uu_eu_{e_\xi} + Uw_eu_{e_\zeta} + Wu_{e_\zeta} + \text{curvature terms} = -g^{11}(G_\xi - TS_\xi) - g^{12}(G_\eta - TS_\eta) - g^{13}(G_\zeta - TS_\zeta) + \frac{1}{\rho\sqrt{g}}(\text{viscous terms}) \tag{3}$$

ζ-momentum equation:

$$\frac{1}{\rho\sqrt{g}}\left\{\frac{\partial}{\partial\xi}[\rho\sqrt{g}(U^2+U)u_ew_e] + \frac{\partial}{\partial\xi}(\rho\sqrt{g}(U+1)Wu_e) + \frac{\partial}{\partial\eta}(\rho\sqrt{g}Uvw_e) + \frac{\partial}{\partial\eta}(\rho\sqrt{g}vW) + \frac{\partial}{\partial\zeta}[\rho\sqrt{g}(U^2+U)w_e^2] + \frac{\partial}{\partial\zeta}[\rho\sqrt{g}(2U+1)Ww_e] + \frac{\partial}{\partial\zeta}(\rho\sqrt{g}W^2)\right\} + Uu_ew_{e_\xi} + Uw_ew_{e_\zeta} + Ww_{e_\zeta} + \text{curvature terms} = -g^{31}(G_\xi - TS_\xi) - g^{32}(G_\eta - TS_\eta) - g^{33}(G_\zeta - TS_\zeta) + \frac{1}{\rho\sqrt{g}}(\text{viscous terms}) \tag{4}$$

Normal momentum equation:

$$Uu_ev_\xi + (Uw_e + W)v_\zeta + \text{curvature terms} = -g^{21}(G_\xi - TS_\xi) - g^{22}(G_\eta - TS_\eta) - g^{23}(G_\zeta - TS_\zeta) \tag{5}$$

where

$$G = \frac{\gamma}{\gamma-1}\frac{p}{\rho} + \frac{1}{2}g^{ij}u_e^iu_e^j$$

The energy equation may also be included in the composite velocity system as an equation for temperature. In the present calculations, however, it is replaced with the assumption of constant total enthalpy. This is a valid approximation for the Mach number regime being considered. The new variable G that appears in these equations is similar to the total (or Bernoulli-like) pressure; G is not, however, assumed to be constant but is calculated from the solution procedure.

In viscous regions, the composite velocity formulation is representative of the reduced form of the NS equations. The continuity, ξ-momentum, and ζ-momentum equations determine U, W, and Φ. The temperature T is obtained from the energy equation (or total enthalpy H), and the total pressure correction is determined from the η-momentum equation. In the inviscid limit as U, $W \to 0$, the continuity equation reduces to the full-potential equation and the Bernoulli relation, G = const, is recovered from the momentum equations. Thus Eqs. (3–5) are identically satisfied, and the composite velocity system reduces to the expected representation for an inviscid, irrotational flow.

The composite velocity scheme is formulated to provide full Euler solutions for the outer inviscid flow. However, if the momentum equations are solved in the present nonconservation form Eqs. (3) and (4), the full potential solution is recovered for the outer inviscid flow instead, i.e., neither entropy nor vorticity is generated in the outer inviscid flow. This includes flows with captured shock waves. To capture the rotational or Euler shock wave in transonic flows, the ξ-momentum and ζ-momentum equations must be written in a quasiconservation form[6] as follows:

ξ-momentum equation:

$$\frac{1}{\rho\sqrt{g}}\left\{\frac{\partial}{\partial\xi}[\rho\sqrt{g}(U^2+2U)u_e^2] + \frac{\partial}{\partial\eta}(\rho\sqrt{g}Uvu_e) + \frac{\partial}{\partial\zeta}[\rho\sqrt{g}(U^2+2U)u_ew_e] + \frac{\partial}{\partial\zeta}[\rho\sqrt{g}(U+1)Wu_e]\right\} + \text{curvature terms} = -\frac{1}{\rho}(g^{11}p_\xi + g^{12}p_\eta + g^{13}p_\zeta) - \frac{1}{\rho\sqrt{g}}\left[\frac{\partial}{\partial\xi}(\rho\sqrt{g}u_e^2) + \frac{\partial}{\partial\eta}(\rho\sqrt{g}vu_e) + \frac{\partial}{\partial\zeta}(\rho\sqrt{g}u_ew_e)\right] - \text{curvature terms} + \frac{1}{\rho\sqrt{g}}(\text{viscous terms}) \tag{6}$$

ζ-momentum equation:

$$\frac{1}{\rho\sqrt{g}}\left\{\frac{\partial}{\partial\xi}[\rho\sqrt{g}(U^2+2U)u_ew_e] + \frac{\partial}{\partial\xi}(\rho\sqrt{g}(U+1)Wu_e) + \frac{\partial}{\partial\eta}(\rho\sqrt{g}Uvw_e) + \frac{\partial}{\partial\eta}(\rho\sqrt{g}vW) + \frac{\partial}{\partial\zeta}[\rho\sqrt{g}(U^2+2U)w_e^2] + \frac{\partial}{\partial\zeta}[2\rho\sqrt{g}(U+1)Ww_e] + \frac{\partial}{\partial\zeta}(\rho\sqrt{g}W^2)\right\} + \text{curvature terms} = -\frac{1}{\rho}(g^{11}pl_\xi + g^{12}p_\eta + g^{13}p_\zeta) - \frac{1}{\rho\sqrt{g}}\left[\frac{\partial}{\partial\xi}(\rho\sqrt{g}u_ew_e) + \frac{\partial}{\partial\eta}(\rho\sqrt{g}vw_e) + \frac{\partial}{\partial\zeta}(\rho\sqrt{g}w_e^2)\right] - \text{curvature terms} + \frac{1}{\rho\sqrt{g}}(\text{viscous terms}) \tag{7}$$

The η-momentum equation, Eq. (5), is retained in nonconservation form and represents the Crocco equation that relates entropy to vorticity.

With the equations in conservation form, the correct entropy rise at the shock wave will now be generated; however, spurious entropy is also generated in nonshock regions. In the present technique, a simple solution to this problem is available. The nonconservative form of the momentum equations, Eqs. (3-5), produces no entropy but accurately convects the entropy or vorticity present in the flow. Therefore, this form of the axial momentum equation is used everywhere except in the shock region where Eqs. (6) and (7) are required. This leads to a solution procedure with the desirable feature of generating the correct entropy rise at the shock wave but not creating spurious entropy in other regions of the flow. The advantage of nonconservative equations away from shock waves and combined conservative/nonconservative systems has been discussed in several studies by other investigators.[9]

Boundary Conditions

Boundary conditions for the composite velocity formulation may be easily specified. At solid surfaces, the no-slip condition and zero injection conditions are used giving $U=-1$, $W=0$, and $v=0$. The upper boundary is to be sufficiently far from the body that the flowfield is undisturbed. This yields freestream boundary conditions $U=0$, $W=0$, $\Phi=\Phi_{fs}$, $T=1$, and $S=0$. At the outflow, $\xi=\xi_m$, only one boundary condition needs to be applied, $\Phi_{\xi\xi}=0$. This, in effect, assumes a weak viscous/inviscid interaction. At the inflow boundary, uniform flow is assumed for all values except at solid boundaries where the no-slip condition is applied. For all geometries presented in this paper, two planes of symmetry exist in the azimuthal direction. In each of these planes, symmetry conditions are applied for U, Φ, T, S, with antisymmetry conditions for W.

Numerical Procedure

The numerical procedure developed for the composite velocity equations is motivated by numerical procedures for potential flows Φ and for boundary-layer flows, U and W. In the composite equations, the upstream or acoustic influence is contained wholly in the potential part of the equations, i. e., $\Phi_{\xi\xi}$. A standard plane relaxation procedure similar to that for solutions to the full potential equation is used for all Φ derivatives. The viscous velocities U and W are treated as boundary-layer velocities and may be marched except in regions of separated flow. The continuity, ξ-momentum, and ζ-momentum equations are solved as a coupled set of equations for U, W, and $\Delta\Phi$. The η-momentum equation and energy equation are solved uncoupled from the system for entropy S and temperature T.

Finite Difference Equations

The composite velocity equations are differenced so that second-order accuracy is obtained for all terms. First-order accurate differencing for the streamwise derivatives U_ξ and W_ξ is left as an option. The difference form of the continuity, ξ-momentum, and ζ-momentum equations is obtained at (i,j,k), with central differences at half-points. The derivatives of Φ are then central differenced at the half point locations. This provides the usual three-point central difference for $\Phi_{\xi\xi}$, $\Phi_{\eta\eta}$, and $\Phi_{\zeta\zeta}$. In the η-ζ cross plane, the values of U and W at the half points are determined by averaging the values at neighboring grid points. To provide the proper upwind bias, consistent with the boundary-layer marching character of U and W, the values of U and W at $i+\frac{1}{2}$ and $i-\frac{1}{2}$ are represented with upwind approximations as follows:

$$U_{i+\frac{1}{2}} = U_i + \tfrac{1}{2}\,\epsilon\sigma_i(U_i - U_{i-1}) \tag{8a}$$

$$U_{i-\frac{1}{2}} = U_{i-1} + \tfrac{1}{2}\,\epsilon\sigma_{i-1}(U_{i-1} - U_{i-2}) \tag{8b}$$

where $\epsilon=0$ provides a first-order accurate representation, and $\epsilon=1$ provides a second-order accurate representation.

In separated flows, the representation of $W_{i+\frac{1}{2}}$ and $W_{i-\frac{1}{2}}$ must be modified to provide the proper upwinding for the W_ξ derivative. This is required since W appears as an additive term in the composite representation for w, rather than as a term multiplying an inviscid velocity, e.g., U. Therefore the only upstream influence in separated regions comes through upwinding of the W_ξ derivative. The representations for $W_{i+\frac{1}{2}}$ and $W_{i-\frac{1}{2}}$ become

$$W_{i+\frac{1}{2}} = SM \times \left[W_i + \frac{1}{2}\,\epsilon\sigma_i(W_i - W_{i-1}) \right] + SP \times \left[W_{i+1} + \frac{\epsilon}{2\sigma_{i+1}}\,(W_{i+1} - W_{i+2}) \right] \tag{9a}$$

$$W_{i-\frac{1}{2}} = SM \times \left[W_{i-1} + \frac{1}{2}\,\epsilon\sigma_{i-1}(W_{i-1} - W_{i-2}) \right] + SP \times \left[W_i + \frac{\epsilon}{2\sigma_i}\,(W_i - W_{i+1}) \right] \tag{9b}$$

where

$$SM = \tfrac{1}{4}[2 + SGN(U_{i-1}+1) + SGN(U_i+1)]$$

$$SP = \tfrac{1}{4}[2 - SGN(U_{i-1}+1) - SGN(U_i+1)]$$

In Eqs. (9a) and (9b), a backward difference for W_ξ results if $SM=1$ and $SP=0$, and a forward difference results when $SM=0$ and $SP=1$. At separation and reattachment points, $SM=\frac{1}{2}$ and $SP=\frac{1}{2}$, giving a central difference for W_ξ. This provides for a smooth transition between backward and forward differencing at separation and reattachment points.

The first-order boundary-layer viscous terms are treated implicitly and have been linearized by assuming all known inviscid velocities u_e, v, and w_e. Since the second-order boundary-layer terms are small, these terms have been included as an explicit correction, with the inviscid velocities calculated from the previous global iteration and U and W determined from previous marching steps. The combinations $G_\xi - TS_\xi$, $G_\eta - TS_\eta$, and $G_\zeta - TS_\zeta$ also have a minimal influence on the solution of the governing equations. These terms have been uncoupled from the momentum equations and are assumed to be known from the previous global iteration.

Certain terms must also be lagged so that a stable relaxation procedure is obtained. In the global relaxation process, the only term that introduces Φ at two different iteration levels is $\Phi_{\xi\xi}$. All first derivatives of Φ in the streamwise direction Φ_ξ and the cross derivatives $\Phi_{\xi\eta}$ and $\Phi_{\xi\zeta}$ are taken from the previous global iteration. All η-ζ cross derivatives are assumed to be known so that a five-point computational star is maintained in the cross plane.

When solving the difference form of the equations, errors arise in the freestream because of incomplete cancellation of metric terms.[10] Essentially, a group of terms that analytically should be zero introduces an error owing to the differencing of metric terms. The following residual term represents the freestream error for the continuity (i. e., full potential) equation

$$FSR = \frac{\partial}{\partial\xi}(\rho\sqrt{g}u_{e_{fs}}) + \frac{\partial}{\partial\eta}(\rho\sqrt{g}v_{fs}) + \frac{\partial}{\partial\zeta}(\rho\sqrt{g}w_{e_{fs}}) \tag{10}$$

where the freestream velocities are calculated from Φ_{fs}. To reproduce freestream results exactly, this error term is subtracted out of each equation.

The η-momentum equation is solved uncoupled. It is treated as a first-order differential equation for entropy S. The difference form of the equation is centered at $i-\frac{1}{2}$, $j+\frac{1}{2}$ with all terms being central differenced at this location. The terms arising from nonorthogonal grids $G_\xi - TS_\xi$ and $G_\zeta - TS_\zeta$ are

taken from the previous global iteration. All other terms in the equation involve U, W, and Φ, which have already been calculated.

Employing the assumptions for a plane relaxation procedure, the final 3×3 system of difference equations to be solved at each cross plane is written as

$$A\Psi^{n+1}_{i,j-1,k} + B\Psi^{n+1}_{i,j,k} + C\Psi^{n+1}_{i,j+1,k} + D\Psi^{n+1}_{i,j,k-1} + E\Psi^{n+1}_{i,j,k+1} = G - F\Psi^{n+1}_{i-1,j,k} - H\Psi^{n}_{i+1,j,k} \quad (11)$$

where $n+1$ represents the current iteration level, n represents the previous global iteration, and $\Psi = [U, W, \Delta\Phi]^T$. Once Eq. (11) has been solved, the values of $T_{i-\frac{1}{2},j,k}$ and $S_{i-\frac{1}{2},j,k}$ are then updated from the energy and η-momentum equations, respectively.

The composite velocity scheme for the RNS equations as currently implemented requires the global storage of three variables: Φ, T, and S. Thus two additional variables must be stored globally to obtain viscous solutions as opposed to potential solutions. If memory restrictions become a consideration, the η-momentum and energy equations may be coupled into the system, thereby removing the need to store T and S. Therefore a viscous solution can be obtained while requiring only the memory needed for a potential solution plus the additional storage of W in the separated flow regions.

Consistent, Coupled, Strongly Implicit Procedure

To solve the system of difference equations, Eq. (11), in an efficient and robust manner, a solution algorithm that is noniterative, unconditionally stable, and spatially consistent is required. A noniterative algorithm is important since this algorithm is applied at each cross plane in the marching direction, and a number of global iterations is required to obtain a converged solution. An unconditionally stable and spatially consistent scheme is desirable since grid stretching in the marching direction allows for greater flexibility in resolving important flow features with a minimum number of grid points. A limitation on the step size in the marching direction owing to stability restrictions or the need to maintain the spatial consistency of the scheme would make the number of planes required in this direction prohibitive.

A solution algorithm that satisfies the above requirements is the consistent, coupled, strongly implicit procedure (CCSIP) developed by Khosla and Rubin.[11,12] The consistent CSIP algorithm may be derived from the following recursion relationship:

$$\Psi_{i,j,k} = GM_{j,k} + ET_{j,k}\Psi_{i,j-1,k} + FT_{j,k}\Psi_{i,j,k+1} \quad (12)$$

where $GM_{j,k}$ is a column matrix, and $ET_{j,k}$ and $FT_{j,k}$ are 3×3 matrices. Equation (12) is substituted into Eq. (11) for $\Psi_{i,j+1,k}$ and $\Psi_{i,j,k-1}$. The corner points introduced in this substitution are represented as follows:

$$\Psi^{n+1}_{i,j+1,k+1} = \Psi^{*}_{i,j+1,k+1} - \alpha(\Psi^{*}_{i,j+1,k} + \Psi^{*}_{i,j,k+1} - \Psi^{*}_{i,j,k}) + \alpha(\Psi^{n+1}_{i,j+1,k} + \Psi^{n+1}_{i,j,k+1} - \Psi^{n+1}_{i,j,k}) \quad (13a)$$

$$\Psi^{n+1}_{i,j-1,k-1} = \Psi^{*}_{i,j-1,k-1} - \alpha(\Psi^{*}_{i,j-1,k} + \Psi^{*}_{i,j,k-1} - \Psi^{*}_{i,j,k}) + \alpha(\Psi^{n+1}_{i,j-1,k} + \Psi^{n+1}_{i,j,k-1} - \Psi^{n+1}_{i,j,k}) \quad (13b)$$

where $\Psi^{*}_{i,j,k} = [U^{*}_{i,j,k}, W^{*}_{i,j,k}, 0]^T$ with U^* and W^* determined from previous marching locations and $0 \le \alpha \le 1$. The consistent form of the solution algorithm is obtained when $\alpha = 1$. After substitution, the terms in Eq. (11) may be regrouped giving relations for $GM_{j,k}$, $ET_{j,k}$, and, $FT_{j,k}$. A simple two-pass inversion procedure may now be used to, determine the solution in the cross plane.

The CCSIP in its present form, Eq. (12), is not a symmetric algorithm. This asymmetry in the algorithm generates asymmetries in the cross-plane solution for three-dimensional geometries. These asymmetries in the cross-plane solution can lead to a procedure that is globally divergent. Symmetric solutions may be restored by iteration on the corner points, Eqs. (13a) and (13b). A large number of iterations at each cross plane is required to restore the symmetry of the solution, however. A better means of obtaining symmetric solutions is to solve the CCSIP algorithm in alternate sweep directions by solving the mirror of Eq. (12). Symmetric solutions may be obtained in the most efficient manner by solving the two alternating directions once and averaging the two solutions. This provides for a symmetric solution with a minimum amount of work, requiring the equivalent of only one local iteration.

Initial Conditions and Convergence Acceleration

We have found the present relaxation procedure for the RNS equations to be sensitive to the initial guess for Φ; the assumption of uniform flow is generally inadequate as an initial condition. This sensitivity arises mainly due to the lack of a time term in the present equations, which provides some temporal damping during the initial transients. Since there is no time term for the viscous velocities U and W, Δt may not be used to control their growth as in time-dependent algorithms. Time terms may be added to the equations, but this degenerates the efficiency of the space-marching algorithm. A better solution to the problems associated with the initial conditions is starting the viscous solution with the corresponding solution to the inviscid full-potential equation. This initial guess may be obtained by solving the inviscid form of the composite velocity equations with slip boundary conditions. An attractive alternative to using the composite system for the potential flow is to use a more efficient code developed strictly for the full-potential equation. The composite velocity procedure may then be used to efficiently determine the viscous solution to the problem.

The convergence of the global relaxation procedure for the composite velocity system is determined primarily by the convergence rate for the inviscid flow variable Φ. It is well known that plane relaxation procedures slow down dramatically as the number of planes in the marching direction is increased. In the present calculations, solutions are always obtained on the coarsest possible grid; subsequent solutions on finer grids are then initiated with the coarser grid solutions. This allows for more rapid upstream propagation of downstream information.

The previous discussion suggests that convergence could be greatly accelerated using a formal multigrid procedure. Multigrid procedures are particularly appealing for the composite velocity system since the inviscid solution is based on the full-potential equation. A unidirectional multigrid procedure has already been developed by Himansu and Rubin[13] for the RNS equations in primitive variable form. This technique can be adapted easily for the composite velocity system.

The convergence of the potential flow may also be accelerated by using overrelaxation for the calculation of $\Delta\Phi$ in the continuity (i. e., full potential) equation.[14] This introduces a time like term $\Phi_{\xi t}$ that provides temporal damping to the system. This additional damping aids in accelerating the convergence of the inviscid flow while introducing no additional error in the converged state.

Transonic Flow and Turbulence Model

Since the outer inviscid solution of the composite velocity system is based on the full potential equation, techniques for treating the transonic full potential equation may be adopted for the composite velocity system. The flux-biasing procedure of Enquist-Osher,[15] which specifies a modified density for the full potential equation, is used for the present calculations. This is a simple scheme that has several advantages. The scheme provides monotone profiles through captured shock waves. The captured shocks are very sharp with only a two-

point transition through the shock wave. The flux-biasing scheme also accurately monitors sonic conditions while transitioning through sonic lines. The theoretical reason for these properties lies in the fact that the Enquist-Osher scheme satisfies an entropy inequality.

The numerical solution of the RNS equations for large Reynolds number flows requires the introduction of a model for turbulence. Algebraic eddy viscosity models provide the simplest means for modeling turbulent flows. Implementing these models requires minimal computer time and storage. The algebraic eddy viscosity model used in the present work was developed by Baldwin and Lomax.[16] This two-layer model is patterned after the Cebeci-Smith turbulence model but removes the need for determining the edge of the boundary layer. For the afterbody configurations calculated herein, the Shang and Hankey relaxation model[17] has been used to account for the memory of turbulence transport. This is required for flows with large adverse pressure gradients.

Results and Discussion

The composite velocity procedure will be used to obtain results for nonaxisymmetric afterbody configurations. To test various aspects of the code, several simpler configurations have also been calculated (see Fig. 1). A sampling of these results will be presented here. A more extensive discussion of these results is given in Refs. 18 and 19.

Axisymmetric Circular Arc Bump

The flow over an axisymmetric circular arc bump is used to test the ability of the present technique to calculate turbulent, transonic flows. The particular geometry chosen has been used by Johnson[20] to evaluate the capabilities of various turbulence models to predict inviscid-viscous interactions that occur at transonic conditions. The test model consists of a circular cylinder having a diameter of 15.2 cm with a circular arc bump having a maximum thickness of 1.9 cm and a chord length of 20.3 cm. The sharp corners at the leading and trailing edge of the bump have been smoothed using a third-order polynomial. By using a grid generation technique that provides for smoother grids than the simple shearing transformation used for the current work, the need for smoothing of the geometry at sharp corners may be eliminated.

In the axial direction, a uniform spacing $\Delta\xi = 0.01667$ is specified on the circular arc bump. A uniform stretching factor of $\sigma = 1.2$ is specified ahead and aft of the bump with the grid extending 4 chord lengths in each direction and a maximum grid spacing of $\Delta\xi = 0.7$. A total of 105 grid points is used in the axial direction with 61 points on the bump and 22 grid points ahead and aft of the bump. An initial spacing at the wall of $\Delta\eta = 0.000025$ is used. The grid spacing at the wall gives a value of $\eta^+ \approx 1$ for the first point away from the wall. The outer boundary is located 6.2 radii from the surface of the cylinder. A total of 61 grid points is used in the normal direction.

Results for a supercritical case $M_\infty = 0.85$ and $Re = 2.03 \times 10^6$ based on chord length are given in Figs. 2 and 3. Comparison of the pressure coefficient with the experimental results of Johnson shows excellent agreement of the shock strength and location. Downstream of the shock, the calculated pressure shows a larger compression than the experimental results in the trailing edge region. From the wall shear results, this is a

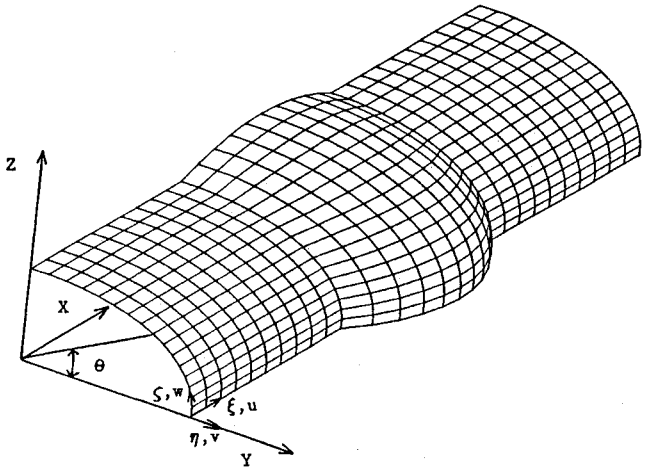

Fig. 1 Simple three-dimensional geometry with a 2:1 elliptical cross section.

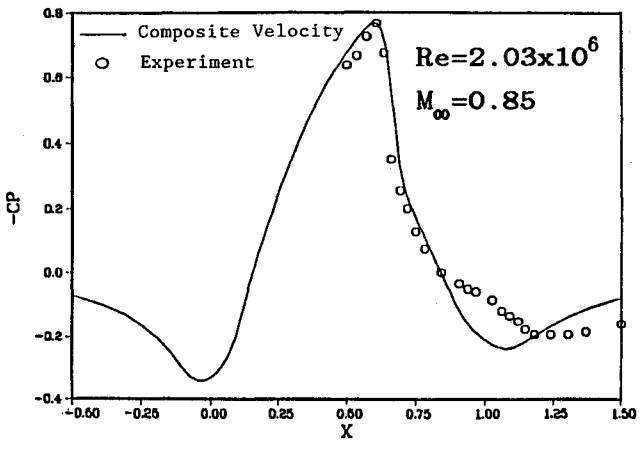

Fig. 3 Pressure coefficient on an axisymmetric circular arc bump: $Re = 2.03 \times 10^6$, $M_\infty = 0.85$.

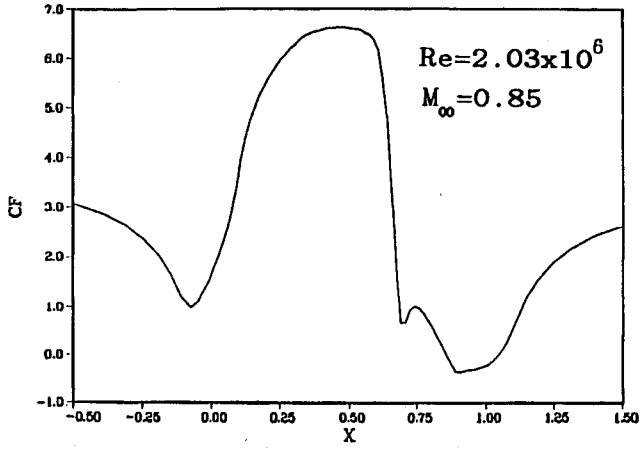

Fig. 2 Wall shear distribution on an axisymmetric circular arc bump: $Re = 2.03 \times 10^6$, $M_\infty = 0.85$.

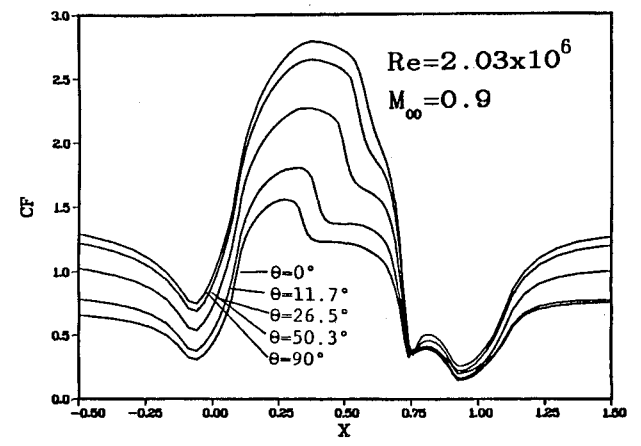

Fig. 4 Wall shear distribution on an elliptic cylinder with a circular arc bump: $Re = 2.03 \times 10^6$, $M_\infty = 0.9$.

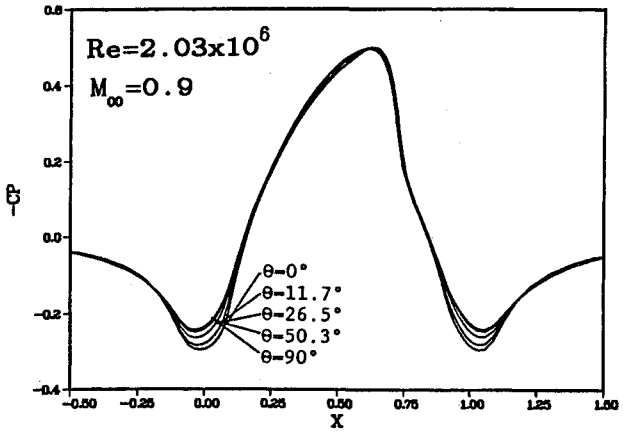

Fig. 5 Pressure coefficient on an elliptic cylinder with a circular arc bump: $Re = 2.03 \times 10^6$, $M_\infty = 0.9$.

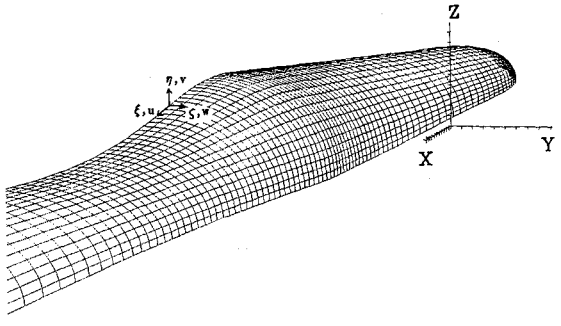

Fig. 6 Nonaxisymmetric afterbody geometry.

region of reverse flow. The computed separation region lies between $x = 0.86$ and 1.04. The experimental results show a separated region of flow between $x = 0.815$–0.85 and 1.1. The variance in the separation point in the experimental results arises from the fact that a rapid increase in the size of the separation bubble occurs at $M_\infty = 0.85$. The experimental results show a slightly larger separated region than the computed results. The discrepancy in the size of the separated flow region and the pressure results in this region is due to the inability of the turbulence model to treat separated flow regions adequately. The smoothing of the trailing edge also reduces the amount of compression of the flow at the trailing edge, causing the computed flow to reattach earlier than the experimental results. This also contributes to the discrepancy in the computed and experimental results downstream of the trailing edge.

Elliptical Cross Section with Circular Arc Axial Variation

For the first three-dimensional flow calculations, a cylinder with a 2:1 elliptical cross section is used. A circular arc variation in the axial direction is specified with the major axis having the same axial variation as the previous axisymmetric geometry. A grid size of $109 \times 61 \times 17$ is used to calculate the present results. A uniform spacing of $\Delta\xi = 0.01667$ is specified on the bump with a grid-stretching factor of 1.2 specified ahead and aft of the bump. The grid is stretched to a maximum grid spacing of $\Delta\xi = 0.125$, which is then held constant. The grid extends 2.27 chord lengths ahead and aft of the body. In the azimuthal direction, a uniform spacing $\Delta\zeta = 0.098$ rad is specified. The normal grid distribution is the same as that used for the axisymmetric calculations.

The flow calculated is for $Re = 2.03 \times 10^6$ and $M_\infty = 0.9$. A turbulent boundary-layer profile is specified at the inflow. The axial variation of the wall shear and the pressure coefficient for several azimuthal locations is given in Figs. 4 and 5. The wall shear shows a substantial variation in the azimuthal direction whereas the pressure coefficient shows less variation except near the leading and trailing edge. The shock strength and location show very little variation in the azimuthal direction.

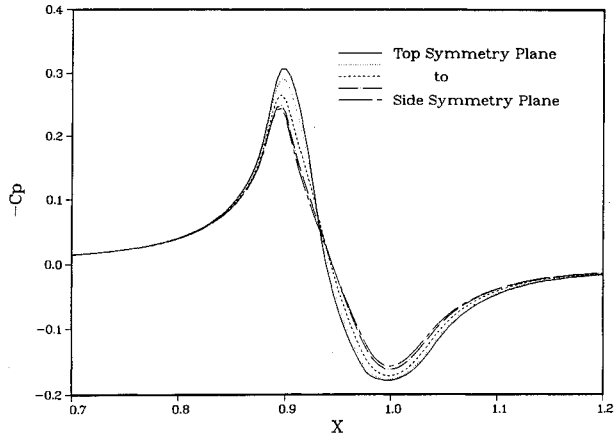

Fig. 7a Pressure coefficient on the afterbody configuration: $Re = 1.0 \times 10^6$, $M_\infty = 0.8$.

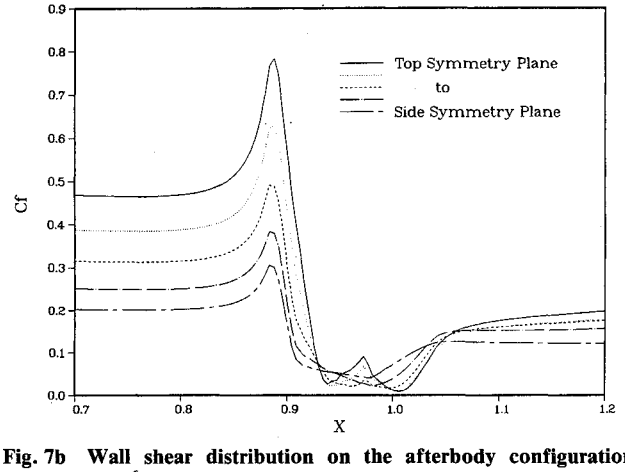

Fig. 7b Wall shear distribution on the afterbody configuration: $Re = 1.0 \times 10^6$, $M_\infty = 0.8$.

The effects of grid resolution in both the axial and azimuthal direction were also investigated for this geometric configuration. The predominant effect of grid refinement is on the wall shear distribution in the region of the shock. Grid refinement has a minimal effect on the pressure coefficient. The effect of second order accuracy for the U_ξ and W_ξ derivatives has also been investigated with the main effect again being on the wall shear distribution in the region of the shock. A more detailed discussion of these results is found in Refs. 18 and 19.

Nonaxisymmetric Afterbody Configuration

The nonaxisymmetric afterbody configuration for which calculations are to be made is shown in Fig. 6. The geometry consists of a main body section with an elliptical cross section of aspect ratio 1.097. The upper symmetry plane transitions to a final boattail angle of 17.6 deg, whereas the side symmetry plane makes a transition to a final boattail angle of 6.7 deg. A solid sting is used to simulate the nozzle exhaust plume. The final aspect ratio of the elliptical cross section is 1.94. A third-order polynomial is used to smooth the discontinuity at the juncture of the boattail with the sting.

The flowfields calculated are doubly symmetric, and only one quarter of the flowfield is calculated. A grid of $146 \times 65 \times 17$ grid points is used. Twenty-eight planes are used to resolve the boattail with the spacing on the boattail being 0.4% of the total body length. Sixty-five grid points are used in the body normal direction with a minimum spacing at the wall of 0.001% of the body length and the outer boundary located approximately one body length away.

The first case calculated for this geometry is for $M_\infty = 0.8$ and $Re = 1.0 \times 10^6$. The flow remains completely subsonic for this freestream Mach number. The pressure coefficient and wall shear distribution for various η = const lines are given in Figs. 7a and 7b. The beginning of the boattail is located at $x = 0.88$. Large azimuthal variations in the pressure and wall shear on the boattail are seen. At the point of minimum pressure, there is a 20% variation in pressure from the top to side symmetry plane. The point of minimum pressure on the side symmetry plane occurs slightly forward of the minimum pressure location on the top symmetry plane.

The methods for accelerating the calculations described earlier were used for these results. A total of 1 h, 25 min, and 22 s of CPU time on the Cray XMP were required for this calculation. Of the total time, 52 min and 11 s or 61% of the time is spent calculating the potential flow used as an initial condition for the viscous calculation. This time can be greatly reduced by using a code designed specifically for calculating potential flows. Thus, with a potential flow solution to the problem, a viscous flow solution may be obtained in only 33 min and 11 s or 38% of the total time required.

The pressure coefficient and wall shear distribution for a transonic case, $M_\infty = 0.9$, are given in Figs. 8a and 8b. A large azimuthal variation in both the pressure and the wall shear distribution can again be seen. The shock wave on the top symmetry plane is much stronger and is located further aft on

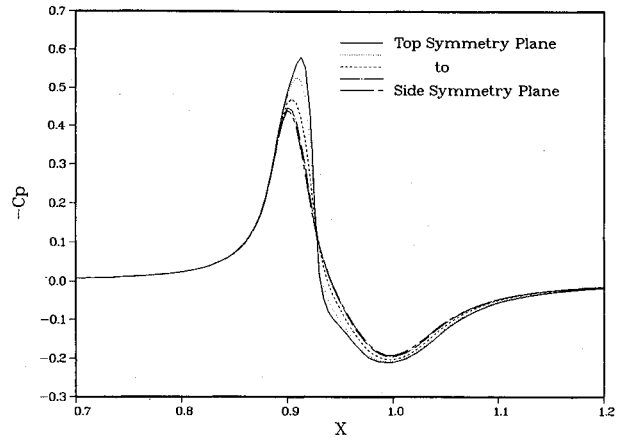

Fig. 8a Pressure coefficient on the afterbody configuration: $Re = 1.0 \times 10^6$, $M_\infty = 0.9$.

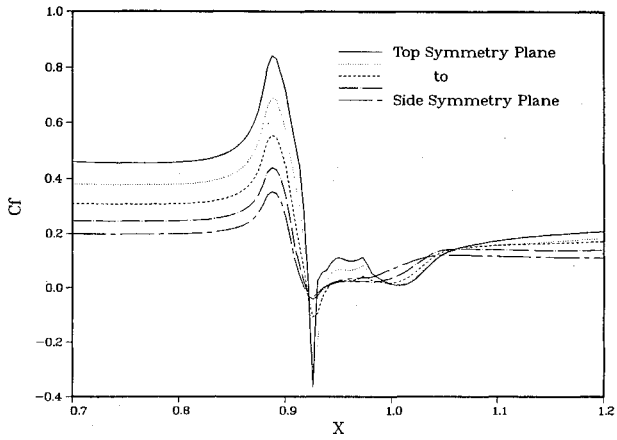

Fig. 8b Wall shear distribution on the afterbody configuration: $Re = 1.0 \times 10^6$, $M_\infty = 0.9$.

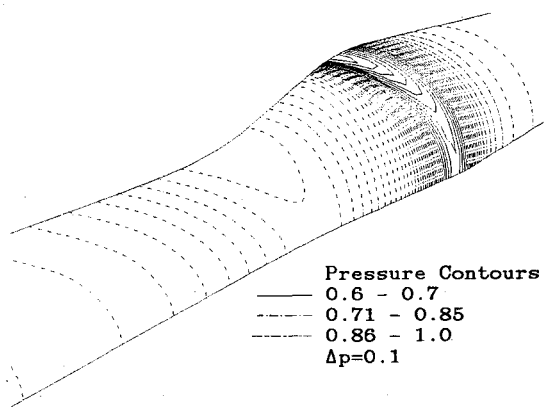

Fig. 9 Surface pressure contours on the afterbody configuration $Re = 1.0 \times 10^6$, $M_\infty = 0.9$.

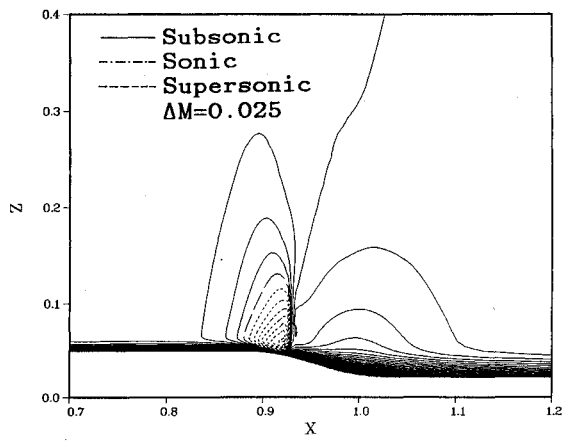

Fig. 10 Mach contours in the top symmetry plane: $Re = 1.0 \times 10^6$, $M_\infty = 0.9$.

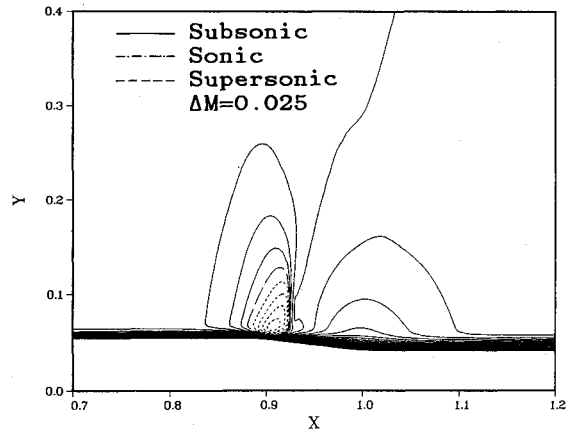

Fig. 11 Mach contours in the side symmetry plane: $Re = 1.0 \times 10^6$, $M_\infty = 0.9$.

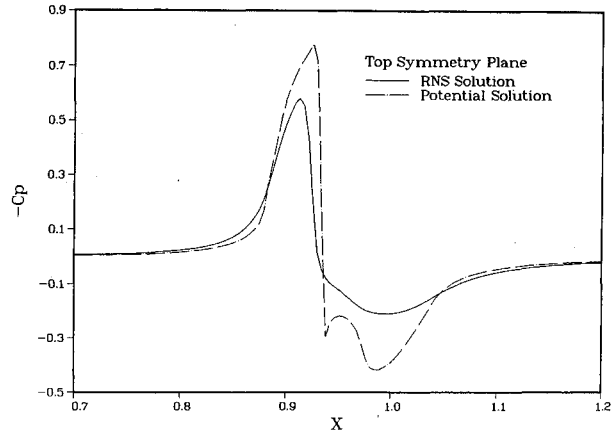

Fig. 12 Effect of viscosity on the surface pressure coefficient: $Re = 1.0 \times 10^6$, $M_\infty = 0.9$.

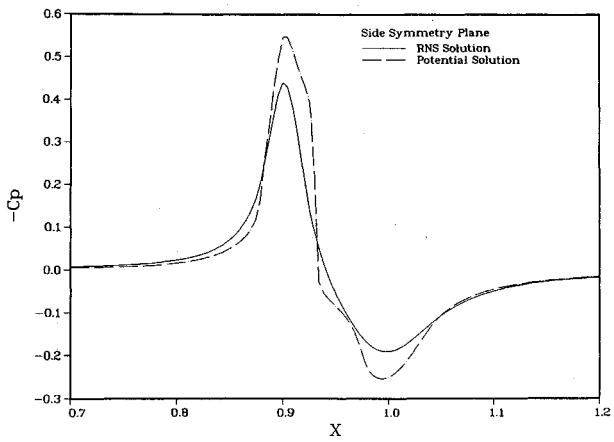

Fig. 13 Effect of viscosity on the surface pressure coefficient: $Re = 1.0 \times 10^6$, $M_\infty = 0.9$.

the boattail. A 24% variation in the minimum pressure is seen. A small region of reverse flow induced by the shock-wave/boundary-layer interaction can be seen in the wall shear distribution just downstream of the shock wave.

Plots of pressure and Mach contours show a clearer picture of the flowfield characteristics. Figure 9 gives surface pressure contours in the boattail region. The expansion region terminating in a shock wave can clearly be seen. This region has a greater axial extent along the top symmetry plane, and the shock wave again appears much stronger. Mach contours in the top and side symmetry planes are given in Figs. 10 and 11, respectively, which clearly show the sharp shock waves generated by the Enquist-Osher flux-biasing procedure. The shock is again much stronger on the top symmetry plane. The effect of the shock on the boundary layer can also be seen, with the boundary layer becoming thinner in the region ahead of the shock and thickening as the boundary layer interacts with the shock wave.

Figures 12 and 13 show the effect of viscosity on the pressure coefficient along the top and side symmetry planes. The viscous effects tend to weaken and diffuse the shock with the viscous shock being located slightly upstream of the potential shock. The viscous flow also undergoes a much smaller compression in the boattail juncture region.

Summary

The present work developed a three-dimensional composite velocity solution procedure for the reduced Navier-Stokes equations. The scheme developed is consistent with both asymptotic boundary-layer and inviscid flow theories and contains all effects of the second-order (or interacting) boundary layer theory and the triple-deck equations. The scheme may be used to model a wide class of strong-interaction flows consistent with these theories, including axial flow separation and strong viscous-pressure interactions. The composite velocity scheme has been differenced to provide second-order accurate solutions. Global storage is required for only three variables. If storage becomes a limiting factor, this may be reduced to one variable by coupling the η-momentum and energy equations to the rest of the system. In separated flow regions, we found that only the W_ξ derivatives needed to be upwinded.

To solve the resulting finite difference equations, a standard plane-relaxation procedure has been used with a consistently coupled, strongly implicit procedure to invert the system at each cross plane. The CCSIP developed is an approximate LU decomposition that provides a solution at each cross plane that is second-order accurate with no iterations on the inversion scheme required. This scheme, coupled with a second order accurate quasilinearization of nonlinear terms, provides a global solution procedure that is second-order accurate.

Results for transonic/turbulent flow over both axisymmetric and nonaxisymmetric geometries have been presented. The composite velocity scheme is an efficient method for solving many three-dimensional problems. Several possible improvements to the algorithm have been pointed out.

Acknowledgments

This research was supported in part by the Air Force Office of Scientific Research under Contract F49620-85-C-0027 and in part under NASA Grant NAG-I-8. The authors wish to thank Joseph Shang for his encouragement, support, and many useful discussions during the course of this work.

References

[1]Rubin, S. G., and Khosla, P. K., "A Composite Velocity Procedure for the Incompressible Navier-Stokes Equations," *Proceedings of the 8th International Conference on Numerical Methods in Fluid Mechanics,* Springer-Verlag, New York, 1982, pp. 448–454.

[2]Khosla, P. K., and Rubin, S. C., "A Composite Velocity for the Compressible Navier-Stokes Equations," *AIAA Journal,* Vol. 21, No. 11, 1983, pp. 1546–1551.

[3]Swanson, R. C., Rubin, S. G., and Khosla, P. K., "Calculations of Afterbody Flows with a Composite Velocity Formulation," AIAA Paper 83-1736, July 1983.

[4]Rubin, S. G., Celestina, M., and Khosla, P. K., "Second-Order Composite Velocity Solutions for Large Reynolds Number Flows," AIAA Paper 84-0172, Jan. 1984.

[5]Gordnier, R. E., "Transonic Viscous and Inviscid Solutions Using a Composite Velocity Procedure," AIAA Paper 86-0074, Jan. 1986.

[6]Gordnier, R. E., and Rubin, S. G., "Transonic Flow Solutions Using a Composite Velocity Procedure for Potential, Euler, and RNS Equations," *Computers and Fluids,* Vol. 17, No. 1, 1989, pp 85–98.

[7]Wilmoth, R. G., and Putnam, L. E., "Subsonic/Transonic Prediction Capabilities for Nozzle/Afterbody Configurations," AIAA Paper 84-0192, Jan. 1984.

[8]Compton, W. B., Thomas, J. L., Abeyounis, W. K., and Mason, M. L., "Transonic Navier-Stokes Solutions of Three-Dimensional Afterbody Flows," NASA TM 4111, July 1989.

[9]Pandolfi, M., "The Merging of Two Different Ideas: A Shock Fitting Performed by a Shock Capturing," *Numerical Methods in Fluid Mechanics, II,* edited by K. Oshima, Japan Society of Computational Fluid Dynamics, Oct. 1986, pp. 372–383.

[10]Shankar, V., Ide, H., Gorski, J., and Osher, S., "A Fast Time Accurate Unsteady Full Potential Scheme," AIAA Paper 85-1512, July 1985.

[11]Khosla, P. K., and Rubin, S. G., "Consistent Strongly Implicit Iterative Procedures," *Proceedings of the 10th International Conference on Numerical Methods in Fluid Dynamics,* Springer-Verlag, New York, June 1986, pp. 375–380.

[12]Khosla, P. K., and Rubin, S. G., "Consistent Strongly Implicit Iterative Procedures for Two-Dimensional Unsteady and Three-Dimensional Space-Marching Flow Calculations," *Computers and Fluids,* Vol. 15, No. 4, 1987, pp. 361–377.

[13]Himansu, A., and Rubin, S. G., "Multigrid Acceleration of a Relaxation Procedure for the RNS Equations," AIAA Paper 87-1145-CP, June 1987.

[14]Bradley, P. F., Dwoyer, D. L., South, J. C., and Keen, J. M., "Vectorized Schemes for Conical Potential Flow Using the Artificial Density Method," *AIAA Journal,* Vol. 24, No. 1, 1986.

[15]Osher, S., Hafez, M., and Whitlow, W., "Entropy Condition Satisfying Approximations for the Full Potential Equation of Transonic Flow," *Mathematics of Computation,* Vol. 44, No. 169, Jan. 1985, pp. 1–29.

[16]Baldwin, B. S., and Lomax, H., "Thin Layer Approximations and Algebraic Model for Separated Turbulent Flows," AIAA Paper 78-257, Jan. 1978.

[17]Shang, J. S., and Hankey, W. L., "Numerical Solutions for Supersonic Turbulent Flow Over a Compression Ramp," *AIAA Journal,* Vol. 13, No. 10, 1975, pp. 1368–1374.

[18]Gordnier, R. E., "A Composite Velocity Procedure for the Three-Dimensional Reduced Navier-Stokes Equations," Ph.D. Dissertation, Department of Aerospace Engineering and Engineering Mechanics, University of Cincinnati, Cincinnati, OH, 1988.

[19]Gordnier, R. E., and Rubin, S. G., "3-D Composite Velocity Solutions for Subsonic/Transonic Flows," *Proceedings of the Fourth Symposium on Numerical and Physical Aspects of Aerodynamic Flows,* Springer-Verlag, New York, Jan. 1989.

[20]Johnson, D. A., "Transonic Separated Flow Predictions with an Eddy Viscosity/Reynolds Stress Closure Model," *AIAA Journal,* Vol. 25, No. 2, 1987, pp. 252–259.